Yokota *et al. Earth, Planets and Space* (2017) 69:172
https://doi.org/10.1186/s40623-017-0754-8

Earth, Planets and Space

FULL PAPER

Open Access

Medium-energy particle experiments–ion mass analyzer (MEP-i) onboard ERG (Arase)

Shoichiro Yokota[1*], Satoshi Kasahara[2], Takefumi Mitani[3], Kazushi Asamura[3], Masafumi Hirahara[4], Takeshi Takashima[3], Kazuhiro Yamamoto[5] and Yasuko Shibano[3]

Abstract

The medium-energy particle experiments–ion mass analyzer (MEP-i) was developed for the exploration of energization and radiation in geospace (ERG) mission (Arase), in order to measure the three-dimensional distribution functions of the inner-magnetospheric ions in the medium energy range between 10 and 180 keV/q. The energy, mass, and charge state of each ion are determined by a combination of an electrostatic energy/charge analyzer, a time-of-flight mass/charge analyzer, and energy-sensitive solid-state detectors. This paper describes the instrumentation of the MEP-i, data products, and observation results during a magnetic storm.

Keywords: ERG, Radiation belts, Medium-energy particles, Mass analyses

Introduction

The exploration of energization and radiation in geospace (ERG) mission, also called Arase after the launch, aims at clarifying the mechanisms for the generation and loss of highly energetic (~ MeV) electrons during space storms and for development of space storms in response to the solar wind disturbance (Miyoshi et al. in preparation). Four electron sensors, two ion sensors, and two fields/wave experiments are mounted on the spacecraft for observing the cross-energy coupling resulting in relativistic electron acceleration/loss and dynamics of the space storms. Medium-energy particle experiments–ion mass analyzer (MEP-i) is one of the ion sensors used for measuring ions in the medium energy range between 10 and 180 keV/q, while the other ion analyzer (LEP-i) covers the energy range less than 25 keV/q (Asamura et al. in preparation). Since the MEP-i measures the three-dimensional energy, mass, and charge state of each incoming ion, the velocity distribution functions for several ion species are obtained separately. The main target of the MEP-i is the ring current ions, which significantly affect the relativistic electron dynamics through the wave-particle interaction as well as the distortion of the global magnetic field.

The ring current ions can generate electromagnetic waves such as magnetosonic waves (Boardsen et al. 1992; Chen et al. 2010) and electromagnetic ion cyclotron (EMIC) waves (Kennel and Petschek 1966; Shoji and Omura 2011), consuming the free energy source of the unstable velocity distribution functions. Since these waves are considered to result in relativistic electron acceleration (Horne et al. 2007) and loss (Horne and Thorne 1998; Summers et al. 1998; Miyoshi et al. 2008), the ion velocity distribution functions in the medium energy range provides key information for obtaining a comprehensive understanding of the energy transfer in the processes responsible for the acceleration and loss of relativistic electrons.

The global ion distribution in the ring current is also important, as it controls the global magnetic field configuration in the inner magnetosphere (Dessler and Karplus 1961), affecting the electron trajectories. The pressure gradient of the medium-energy ions is therefore a key input parameter for modeling the development of storms and electron behavior during the storms.

Ion mass analyses are required for constructing velocity distribution functions and moment parameters for each ion species, providing important information on the

*Correspondence: yokota@ess.sci.osaka-u.ac.jp
[1] Osaka University, Machikaneyama-cho, Toyonaka 560-0043, Japan
Full list of author information is available at the end of the article

variability of ion species in the magnetosphere. Although atomic oxygen ions are the dominant heavy ions of the terrestrial origin, nitrogen ions (Christon et al. 2002; Liu et al. 2005) and heavier molecular ions (Klecker et al. 1986; Yau et al. 1993) were also observed during storm times. There have been studies on escaping processes from the ionosphere and transport in the magnetosphere of these ions (Wilson et al. 1997; Su et al. 1998; Kitamura et al. 2012), although the processes are not fully understood.

In this paper, we present the instrumentation and performance of the MEP-i with observational results obtained during a storm.

Instrumentation

Figure 1 shows a photograph and cross section of the MEP-i flight model. The upper part, which is partially whitened for the heat radiation to the outer space, contains sensor optics, detectors, and electronics boards. The lower part, which is blackened for the thermal coupling inside the spacecraft chassis, has electronic boards including power supply unit boards and a CPU board. The aperture of 360° near the sensor top provides a $4-\pi$ sr field-of-view (FOV) by using the spacecraft spin motion. Incident ions are energy/charge (E/q)-filtered by an electrostatic analyzer (ESA) and pass through ultra-thin carbon foil to knock out secondary electrons, as illustrated in Fig. 1b. The carbon foil is mounted on metal grids of 333 lines per inch with a thickness of ~ 5 nm according to the energy degradation obtained in the laboratory experiments. The ions are finally detected by one of the silicon solid-state detectors (SSDs), while secondary electrons are also generated at the surface of the SSD. Both secondary electrons from the carbon foil and SSD are collected and detected by a microchannel plate (MCP) unit mounted on the center. The time difference between the "start" electrons from the carbon foil and "stop" electrons from the SSD corresponds to the time-of-flight (TOF) of the ions, providing a mass/charge (m/q) when combined with the E/q analyses. Furthermore, the energy (E) information determined by the SSD in combination with E/q and m/q provides m and q if the incident ion energy is sufficient to generate an SSD signal pulse higher than the discrimination level.

The E/q spectra over the medium energy range between 10 and 180 keV/q are obtained by sweeping the high voltages from 0 V to + 5 kV and to − 5 kV, which are applied to the outer and inner electrodes of ESA, respectively. The maximum potential difference of 10 kV = + 5 kV–(− 5 kV) corresponds to 180-keV ion measurements (analyzer constant = 18). The incoming directions are determined by the position-sensitive MCP unit with 16 discrete anodes, enabling the measurements of three-dimensional velocity distribution functions for each ion

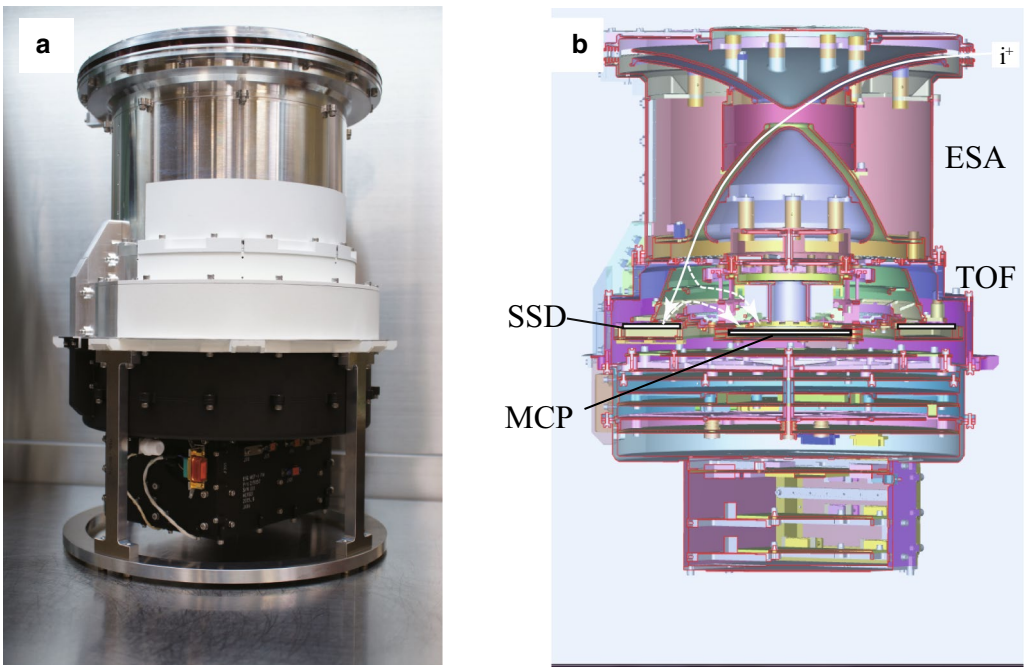

Fig. 1 **a** Photograph and **b** cross-sectional view, of the MEP-i flight model. The anti-sunward side of the analyzer is whitened for heat radiation. Trajectories of incident ions (solid curve) and secondary electrons (dotted curves) are shown in the cross-sectional view

species. The 16-channel SSDs also provide the direction information, resulting in the reduction in accidental coincidence by background noise. Table 1 summarizes the specifications of the MEP-i including the performance of the energy and mass analyses, size, weight, and power consumption.

The MEP-i is mounted on the −X panel of the spacecraft as shown in Fig. 2a. The ERG spacecraft is a sun-pointing and spinning spacecraft with the sun in approximately the −Z direction, with an offset of ~ 10°. Therefore, the azimuthal channels 0 and/or 15 of the MEP-i are intermittently irradiated with the solar EUV flux. The FOV of the MEP-i is partially blocked by the adjacent particle instrument (LEP-e, Kazama et al. 2017) on the same panel, the solar array paddle yokes, and wire-antenna (PWE, Kasahara et al. 2017). The largest FOV blocking, caused by the yokes, is below 10°. The azimuthal channels 0 and 1 are affected by the yokes.

The ESA sweeping voltage (SV) is stepped repeatedly as illustrated in Fig. 2b. It is synchronized with the spacecraft spin except for eclipse times. The spin is divided into 16 phases, each of which holds 16 SV steps. Since the nominal spin period of the ERG spacecraft is ~ 8 s, each SV step has ~ 31 ms [= 8 s/16 (spin phase)/16 (SV step)]. The SV rising time is longer than 10 ms to the full output of ± 5 kV, as illustrated in Fig. 2b, causing the detection of ions of a variety of energies during the first SV step. Therefore, on the ground we exclude the data of the first SV step for scientific analyses. In addition, since there are settling times of several milliseconds in the other SV steps, the MEP-i currently holds "dead time" of 7.215 ms in which the acquisition of data is suspended in each SV step.

The MEP-i block diagram is shown in Fig. 3. The signal processing, data allocation, and supplying of high voltages are controlled by a sensor interface (IF)-field programmable gate array (FPGA), called IF-FPGA. For the ESA energy analyses, the applied voltages are controlled by the IF-FPGA, referring to the tables of the 16-step SV values. Note that the tables can be replaced by commands or the rewriting of the EEPROM data even after the launch. Secondary electrons emitted from the carbon foil due to transmitting ions are detected by the MCP anodes as start signals. For the start signal detections, 16 units of discrete anodes and preamps are equipped. Another 16 units of anodes and preamps handle the stop signals due to the secondary electrons emitted from the SSD surface by the incident ion impact. The time difference between the start and stop signals is converted to a digital value by time-to-digital converters (TDCs). Another FPGA, the TOF-FPGA, reads the digital data and increment corresponding *m/q* counters by referring to the *m/q* table for normal-mode operation (defined in the later section). The IF-FPGA receives the TOF data from TOF-FPGA and sends a trigger to the SSD unit. On the other hand, the SSD unit independently detects incident ions and sends the pulse height data corresponding to *E* when an FPGA in the SSD unit, SSD-FPGA, receives

Table 1 MEP-i performance and specifications

Parameter	Value	Notes
Energy range	10–180 keV/q	
Energy resolution	7%	FWHM
	37%	SV step interval
Analyzer constant	18	
Number of energy steps	16 per spin	The first-step data were not used for scientific analyses due to the slow ramping of SV
Mass discrimination	H^+, He^{++}, He^+, O^{++}, O^+ and O_2^+	
FOV	360° (azimuth) × 2.7° (elevation)	Azimuthal gaps between detectors
	10.5° (azimuth) × 2.7° (elevation) per anode	FWHM
Number of anodes	16	Circularly arrayed
Geometric factor of ESA	2.9×10^{-4} cm^2 sr eV/eV per anode (normal channel)	Calculated in the numerical model
	6.0×10^{-5} cm^2 sr eV/eV per anode (narrow channel)	Calculated in the numerical model
Time resolution	4 s per full 3-D distribution function 500 ms per energy sweep (16 steps) 31.3 ms per energy step	For normal spin of 8 s
Sensor size	φ310 mm × 402 mm	Including an electronics box for the CPU and power supply unit (PSU)
Sensor mass	9.8 kg	
Power consumption	23 W	The efficiency of PSU is 60%
Data size	6.556 kBytes per energy sweep	Before compression and reduction

The resolution is indicated by the full-width at half maximum (FWHM)

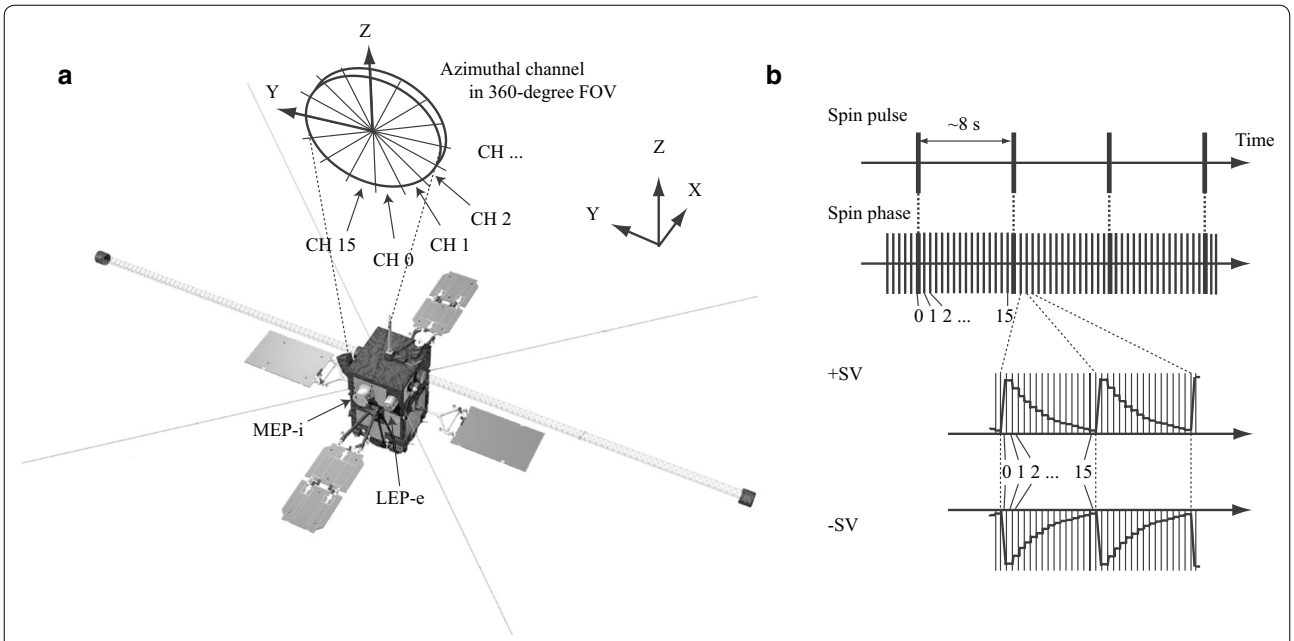

Fig. 2 **a** Mounting position of the MEP-i on the ERG spacecraft, satellite coordinate system, and definition of the MEP-i azimuthal channels. **b** Observation sequence of the spin phase and ESA sweeping voltages of the MEP-i

the trigger from the IF-FPGA. The IF-FPGA also controls high voltages applied to the MCP, TOF, and SSD assemblies via the high-voltage power supply (HVPS) boards. The CPU software transmits commands to the IF-FPGA and receives the observation data from it. After processing, the software sends the packets to the mission data processor for downlink via the mission network. Two power supply units (PSUs) called PSU1 and PSU2 are contained in the sensor package, providing digital 3.3 V and analog ± 12 and 5 V, respectively.

In the following section, we describe the details of the three key components; the ESA, TOF, and SSD for measuring *E/q*, *m/q*, and *E*, respectively. The results of the laboratory tests and comparison with simulations will also be presented in "Cusp-type ESA energy/charge analyses" and "Time-of-flight mass/charge analyses" Subsections.

Cusp-type ESA energy/charge analyses

In order to measure ions in the medium energy range (10–180 keV/q), the MEP-i employs a cusp-type ESA (Kasahara et al. 2006), developed to extend the uppermost energy using a feasible sensor size (see Fig. 4). It holds a much larger analyzer constant compared to the conventional top-hat spherical (Carlson et al. 1982) and toroidal (Young et al. 1988) ESAs. These conventional ESAs are frequently dedicated to measurements of low-energy ($\leq \sim 30$ keV/q) particles and are utilized for ERG mission (Asamura et al. in preparation; Kazama et al. 2017). Although a spherical ESA for the Juno mission covers an energy range of 0.1–100 keV by using the electric field up to 4 kV/mm (McComas et al. 2013), the cusp-type ESA achieves the 180-keV ion measurement with the electric field of 2 kV/mm. The outer and inner bending plates are applied with positive and negative SVs up to + 5 kV and − 5 kV, respectively. The energy and angular responses of the cusp-type ESA are nearly similar to those of spherical and toroidal ESAs (see Fig. 5). Figure 5 also shows agreement of the energy-angular response measured in the laboratory with that calculated in the simulation model. Figure 6 compares the energy and angle responses of 16 azimuthal channels, indicating that the differences of the peak energies and angles are small compared to the nominal energy/angle resolution determined by the SV stepping and spin-phase width (22.5°).

Time-of-flight mass/charge analyses

Incorporation of the TOF *m/q* analyses using carbon foil into the ESA *E/q* analyses has been frequently utilized for space plasma observation (e.g., Williams et al. 1964; Hamilton et al. 1990; Gloeckler et al. 1992; MacDonald et al. 2009), and we recently developed TOF *m/q* analyzers for low-energy ion observation in orbit (Yokota et al. 2005; Delcourt et al. 2016). For the TOF mass analyses, the MEP-i has a flight path length of ~ 48 mm from the carbon foil to the SSD surface as well as 16 sectors of the carbon foil holders and the start and stop anodes (see Figs. 1, 3). The start and stop electrons are collected

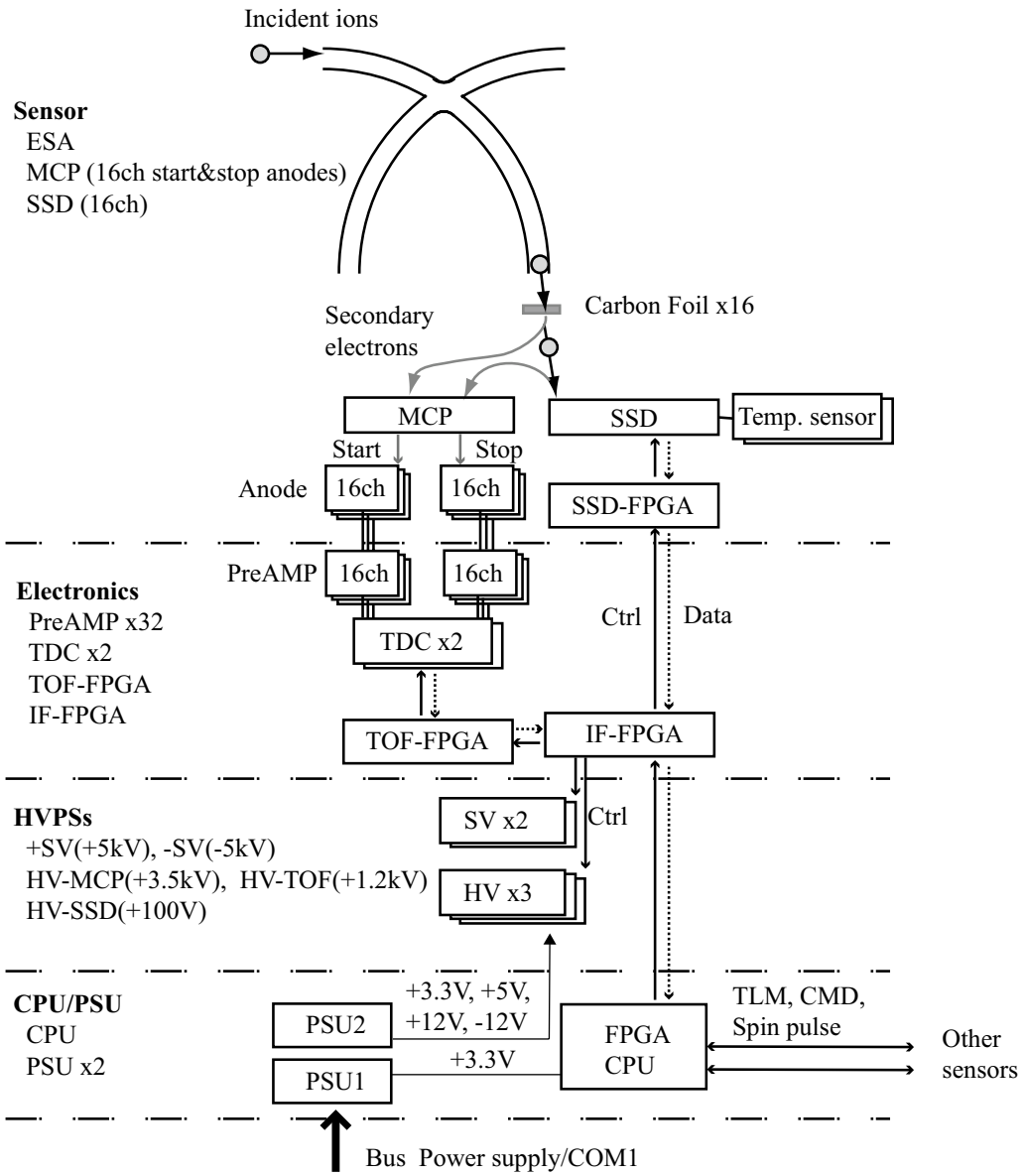

Fig. 3 Block diagram of the MEP-i internal functions

by the MCP surface on which their landing locations are clearly separated (see Fig. 4). In order to reduce the background due to penetrating high-energy particles, the areas of the start and stop anodes are designed to be as small as possible, ~ 90 and ~ 110 mm^2/channel, respectively. This is enabled by a three-dimensional (i.e., non-axisymmetric) structure of the TOF optics. Figure 7 shows two types of carbon foil holders; a normal sector of 12.5-degree width open area and a narrow sector of 2.5-degree width open area. In order to partially offer high angular resolution measurements, the narrow carbon foil holders are mounted only on azimuthal channels 3 and 11 (see Fig. 2a). Figure 8 demonstrates the azimuthal responses for narrow and normal channels obtained through the laboratory tests. The detection efficiencies of the start and stop electrons are calculated from the count rates of the start electron, the stop electron, and their double coincidence. The differences of the detection efficiencies between the start and stop electrons are mostly caused by the ion angular scattering due to the carbon foil. The stop signal efficiencies generally increase for higher energies for any species, since the angular scattering has less effects for faster ions. These detection efficiencies also include the emission rate of

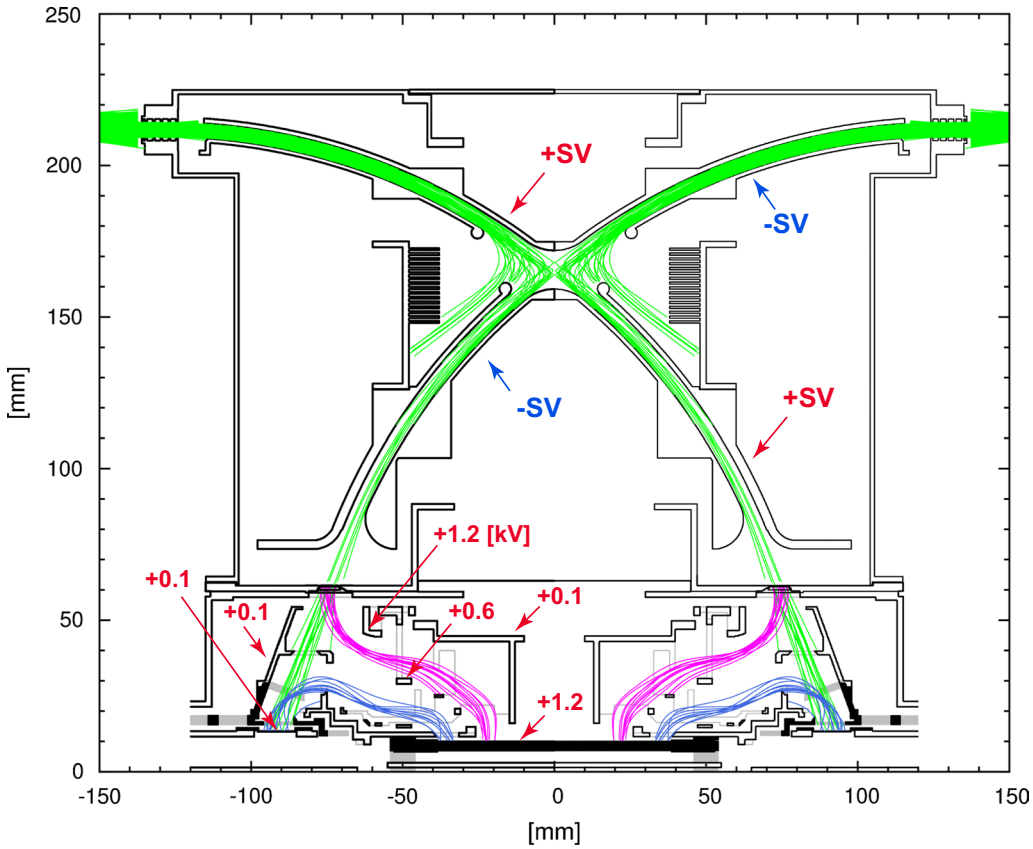

Fig. 4 Ion optics and trajectories of incident ions (green), and the start (purple), and stop electrons (blue) attracted to the MCP surface. All applied voltages are also indicated

these secondary electrons from the carbon foil and SSD surface. In the double-coincidence profiles, the FWHMs are 3.2° and 10.3° for the narrow and normal sectors, respectively.

Figure 9 represents the TOF profiles for various ion species and energies. The incident energies were 10, 40, 80, and 120 keV/q, for species H^+ ($m/q = 1$), $H_2{}^+$ ($m/q = 2$), He^+ ($m/q = 4$), N^+ ($m/q = 14$), and $N_2{}^+$ ($m/q = 28$). The MEP-i holds 512 TOF bins, and the longest window corresponds to 400 ns (0.78125 ns/bin). All measured profiles (color histograms) almost agreed with the calculated ones derived from the numerical model (gray shades) assuming a carbon foil thickness of 5 nm, illustrating that the sensor optics works as expected. Although the peak of $N_2{}^+$ was not calculated in the simulation due to the lack of carbon foil energy straggling data for molecular ions, the laboratory data are useful to evaluate in-flight data. The efficiencies for these ion species and several energies are obtained using double-coincidence data, as shown in Fig. 8. Since the efficiency differences for species and energies are not negligible, the efficiency table will be revised based on both the observation and calibration data.

SSD total energy analyses

For the observation of high-energy particles, SSD energy analyses have been previously combined with TOF techniques (e.g., Williams et al. 1978). The SSDs used for the MEP-i are thin-dead layer silicon-strip detectors (Kasahara et al. 2009) with an effective area of ~ 13 mm × 13 mm and thickness of ~ 100 μm. For the radiation belt exploration, we selected a rather thin chip to avoid the high-count-rate background of gamma-rays generated by MeV electrons via the Bremsstrahlung process. Otherwise, the thickness of more than 300 μm is better for the lower capacitance noise. Another feature of the MEP-i SSD is that the electrodes on the backside (p-side) of the silicon are divided into 16 strips to reduce the surface area. Thus, both the capacitance and leakage current noises are reduced.

Figure 10 illustrates the pulse height (PH) histograms for various ion species and energies measured

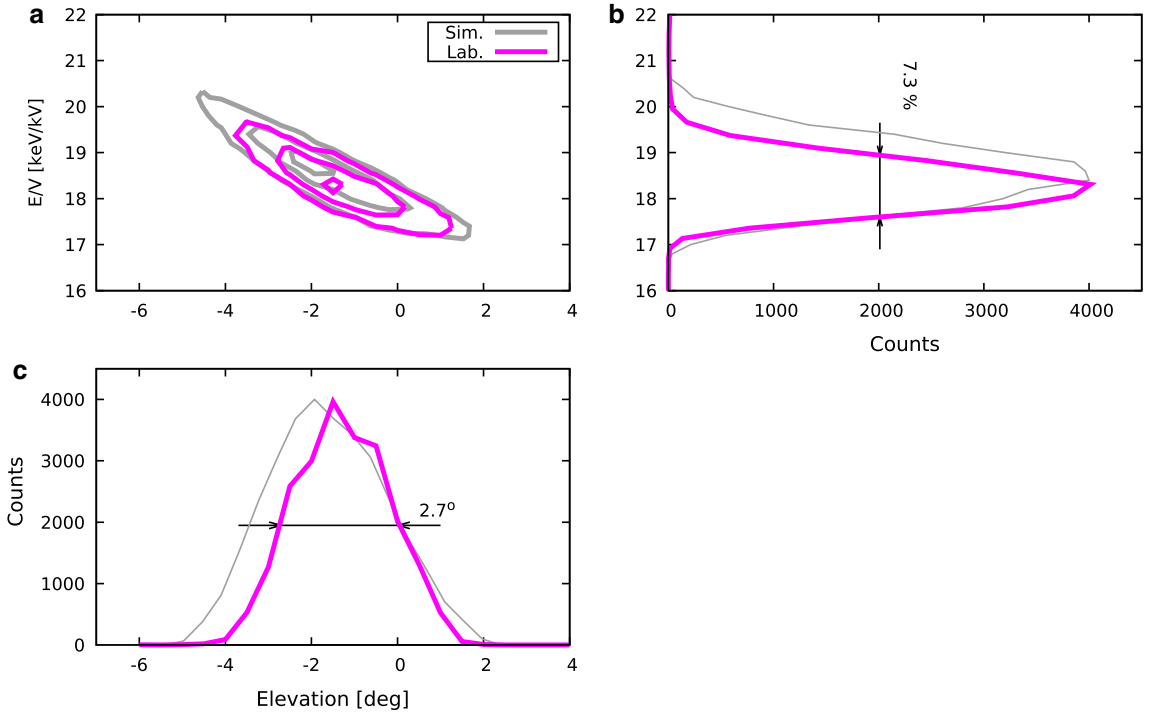

Fig. 5 Measured (Lab.) and calculated (Sim.) energy–angular responses of the azimuthal channel 0 for the 40-keV proton beam

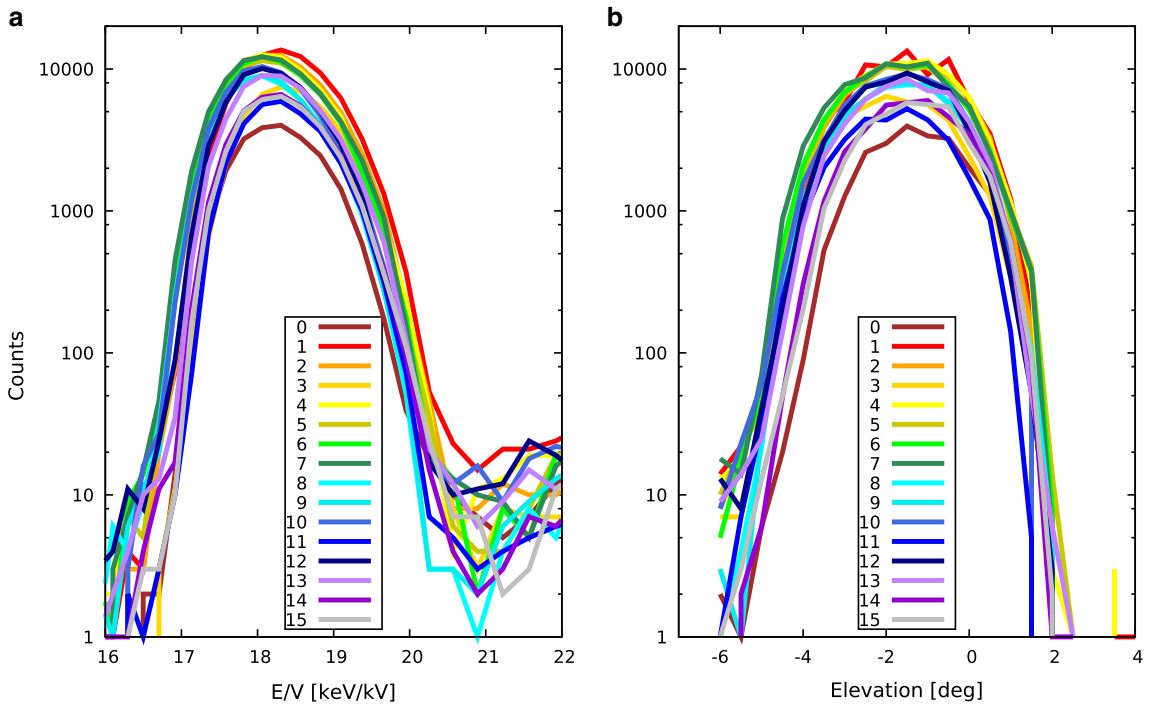

Fig. 6 **a** Energy and **b** angular responses of the 16 azimuthal channels for the 40-keV proton beam measured in the laboratory. The relative counts are not significant because they were dominantly due to the ion beam intensity

Fig. 7 Carbon foil holders for the normal sectors (left) and narrow sectors (right), with open areas of 12.5° and 2.5° in the azimuth, respectively

in the laboratory. The incident energies are 20, 40, 80, and 120 keV/q, for species H^+, $H_2{}^+$, He^+, N^+, and $N_2{}^+$. The PH corresponding to the zero energy is ~ 140, while the discrimination level is ~ 143 expressed by dash line. The conversion factor (gain) from the PH to energy is ~ 2 keV/unit. These measured data were obtained when the SSD temperature was 34 °C, which is rather high compared to that expected in the orbit. (Since this test was conducted in the vacuum and the active cooling was not implemented, the temperature was relatively high). At 20 keV/q, the H^+ peak is much higher than the other peaks and relatively far from the discrimination level (see Fig. 10a). This means that the main component of H^+ is detected, while those of the other species are mostly stopped in the dead layer on the incident surface of the SSD. The detected H^+ also experience significant energy losses in the dead layer, resulting in a detected energy of ~ 10 keV compared with the incident energy of 20 keV. At 40 keV/q, H^+, He^+, and $H_2{}^+$ are detected, as shown in Fig. 10b. The peaks of N^+ and $N_2{}^+$ that are still adjacent to the discrimination level were not main components but high-PH tails. In Fig. 10c, the N^+ peak is clearly separated from the discrimination level, indicating that the N^+ ions mostly penetrated through the dead layer and generated significant PHs in the sensitive region of the SSD at 80 keV/q. The second peak in the $H_2{}^+$ distribution appears because of fragmented H^+ or neutral H signals from the incident $H_2{}^+$. We suggest that one of the fragmented H^+ or H hit the SSD, while the other hit the electrode outside the effective area of the SSD. In that case, the detected energy would be about the half of

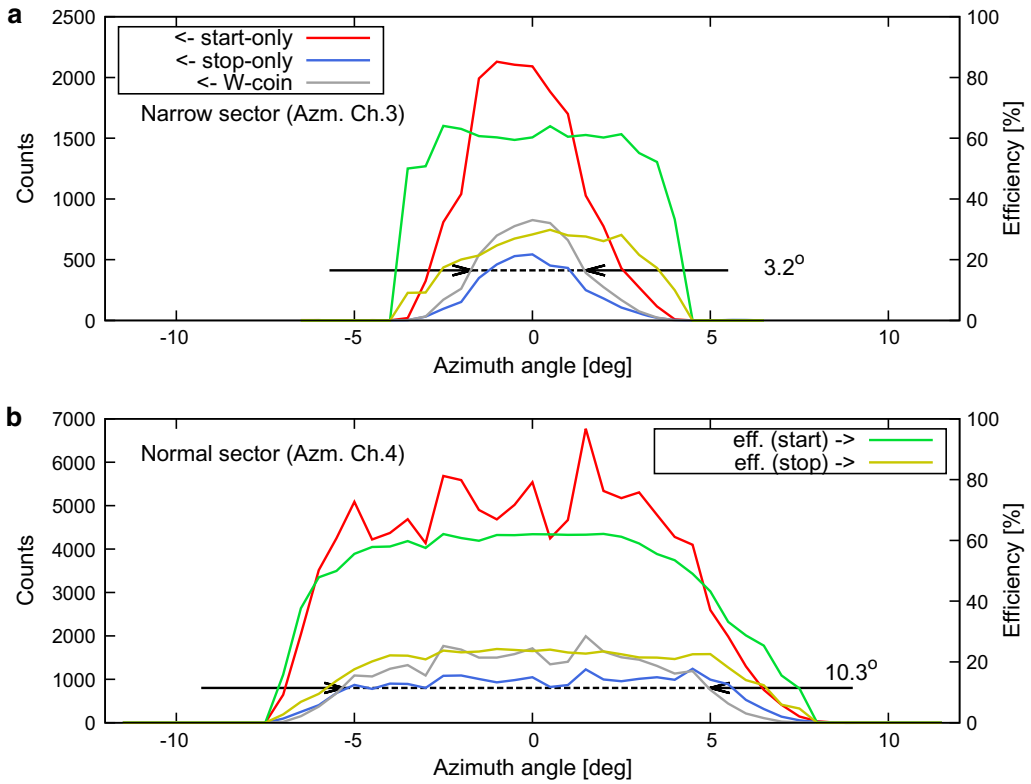

Fig. 8 Dependences of count rates and efficiencies on the incident azimuthal angle for the **a** narrow and **b** normal channels

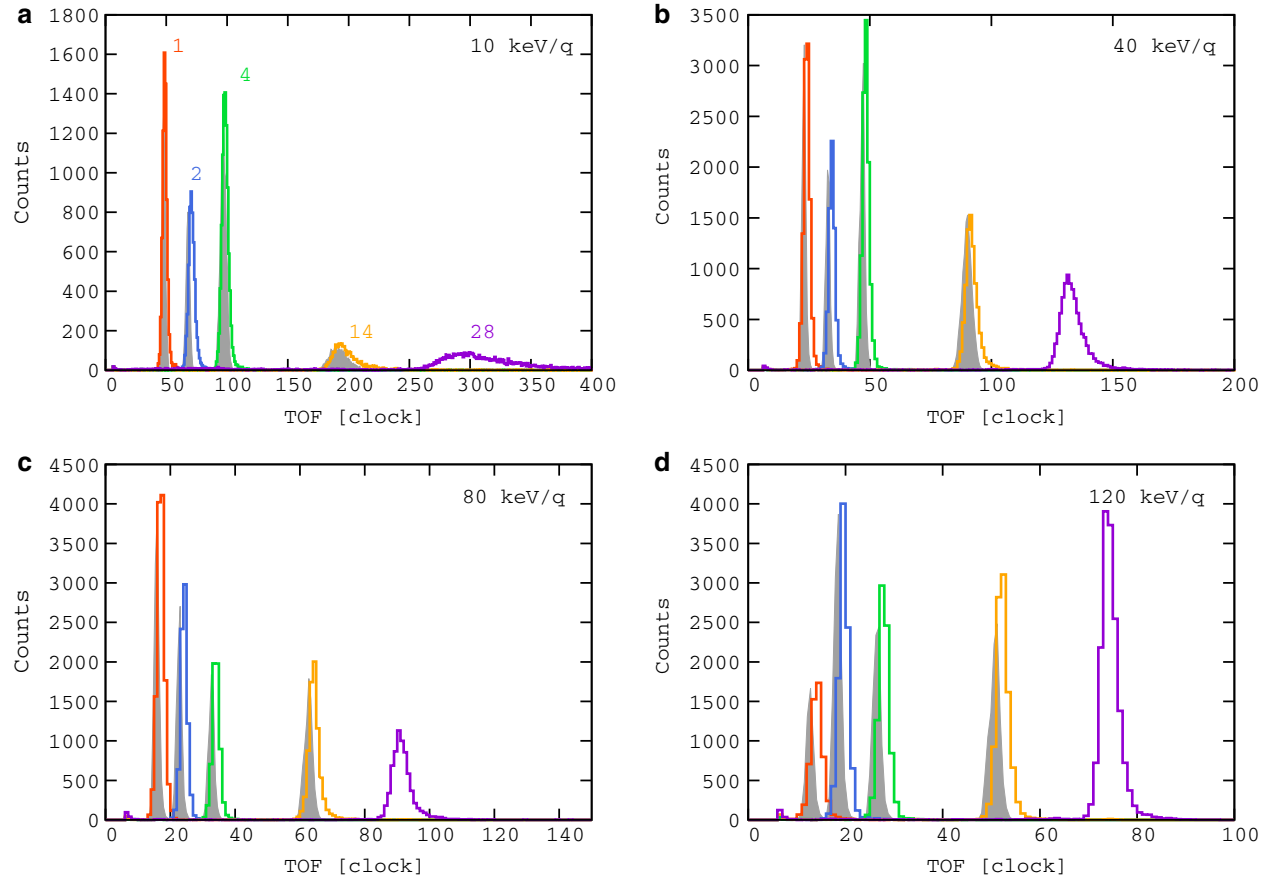

Fig. 9 TOF profiles of azimuthal channel 7 for **a** 10-keV/q, **b** 40-keV/q, **c** 80-keV/q, and **d** 120-keV/q beams of H^+ ($m/q = 1$), H_2^+ ($m/q = 2$), He^+ ($m/q = 4$), N^+ ($m/q = 14$), and N_2^+ ($m/q = 28$). The color histograms indicate the laboratory data, while the gray shades are the results of the numerical simulations assuming the carbon foil thickness of 5 nm. The relative counts are not significant because they are dominantly due to the ion beam intensity. The MEP-i has 512 TOF bins, and the longest wind corresponds to 400 ns (0.78125 ns/bin)

the incident energy, which is consistent with the data. Finally, at 120 keV/q, the N_2^+ ions are detected without a significant number loss and still with significant energy loss (see Fig. 10d).

The PH distributions are clearly mass dependent due to the mass-dependent energy loss at the dead layer (Funsten et al. 2004; MacDonald et al. 2009), as seen particularly at 120 keV/q. However, such SSD PH profiles do not degrade the charge state determination, which is the primary role of the SSDs in the MEP-i, because m/q is determined by the TOF. In addition, the MEP-i SSD provides the PH distribution widths of ~ 20 keV for H^+ and He^+ over 40 keV/q, and that of 40 keV for N^+ over 80 keV/q, resulting in E resolution of ~ 50%. Such an E resolution is sufficient to discriminate He^{++} from H_2^+ and multi-charged oxygen ions from single-charged other ions, by referring to E/q and m/q which are measured within 10 s %. The SSD PH information will be useful for searching minor components such as He^{++} in "list data" described in the next section.

Observation modes and products

The MEP-i has three observation modes, Normal, TOF, and SSD, including an engineering mode. Table 2 shows the data of the three observation modes obtained for each spin-phase channel (~ 0.5 s). The MEP-i is most often operated in the Normal mode, providing the three-dimensional distribution functions for several species. The TOF and SSD modes provide detailed information obtained from the TOF and SSD analyses, respectively.

The sizes of the raw data are also shown in Table 2. The sizes in the telemetry data are actually reduced by a loss-less compression. Since the limitation of the ERG system data recorder sometimes requires the MEP-i to further reduce the data size, we prepared additional reduction modes, as listed in Table 3.

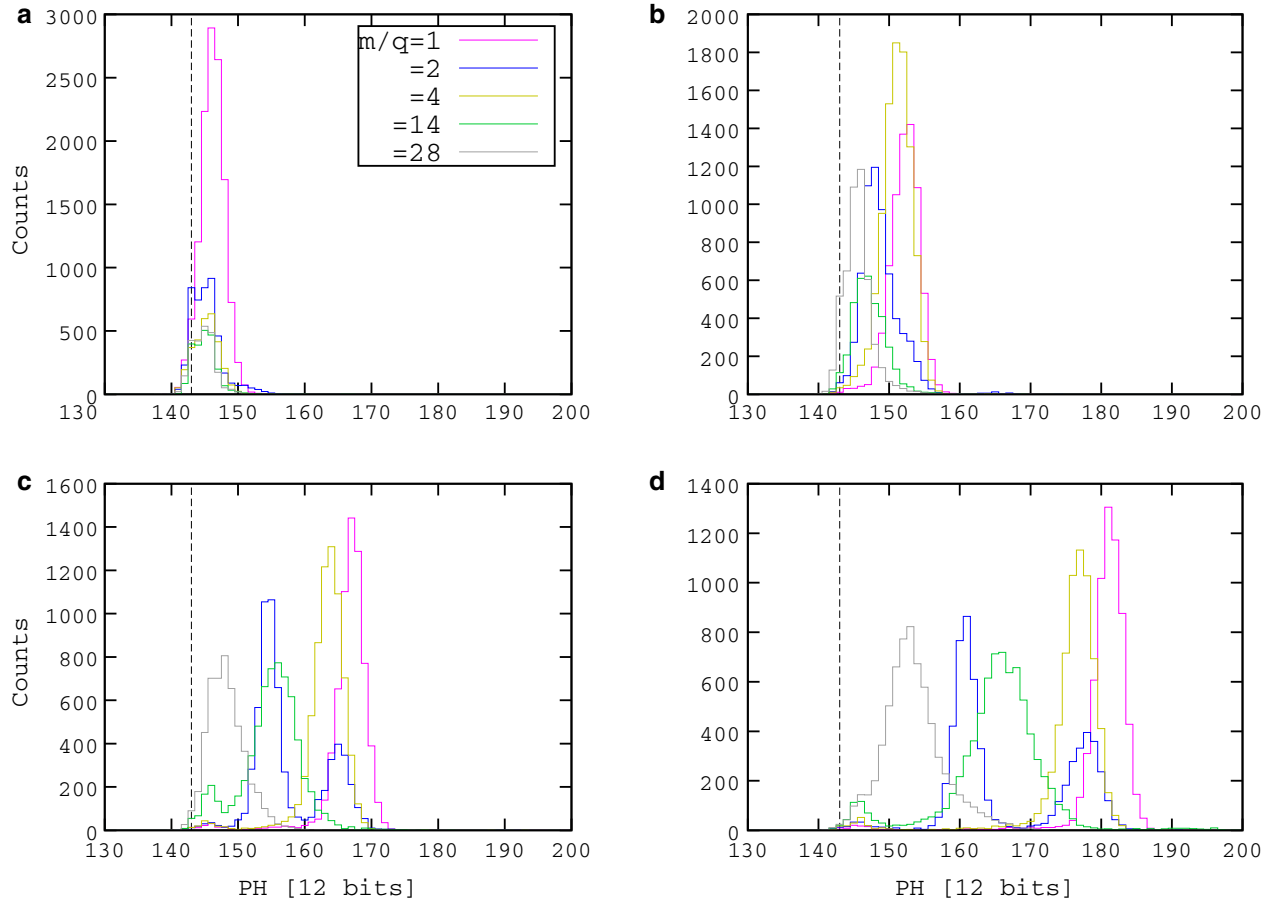

Fig. 10 PH distributions for **a** 20-keV/q, **b** 40-keV/q, **c** 80-keV/q, and **d** 120-keV/q beams of H^+ ($m/q = 1$), H_2^+ ($m/q = 2$), He^+ ($m/q = 4$), N^+ ($m/q = 14$), and N_2^+ ($m/q = 28$). The dashed lines indicate the threshold level

Normal mode

The Normal-mode data consist of the count and list data. Double-coincidence count data are 16-bit depth, for 16 SV steps, azimuthal 16 channels and 8 m/q bins, resulting in a total size of 4096 bytes. The allocation of the 8 m/q bins is performed using the m/q tables which were prepared based on the pre-flight and in-flight calibration data. List data are composed by event data, while the number is limited to 160. Each event of 4 bytes contains the numbers of the SV step, azimuthal channel, TOF channel from the TOF analyses and PH channel from the SSD analyses. The list data are mainly used for in-flight calibrations. Since the MEP-i was designed to have a maximum count rate of ~ 3000 counts/s, for a single azimuthal channel that could generate list data of 1.5 Mbytes, the production of the list data is restricted up to 10 events for each SV step (~ 31 ms) and then the size of the list data is limited to 640 bytes per spin-phase channel.

TOF mode

The TOF mode provides high-resolution (512-channel) TOF data in which the 16 azimuth channels are summed into 4. There are three additional 24-bit counters, start-only, stop-only, and double-coincidence counters for 16 azimuth channels. The TOF mode is used for in-flight calibration, especially for preparing the m/q tables, as well as searching minor ion species. The ESA SV step is kept during one spin phase and the 16 SV steps complete in the one spin period including the 16 spin phases. This operation pattern reduces the data size. As a result, one spin period is required to obtain one energy spectrum. Although this mode also produces the list data, the PH information from the SSD analyses is not available.

SSD mode

The 16-channel energy data allocated by the SSD analyses are available in the SSD mode. The MEP-i excludes the TOF information in this mode to keep the same data size

Table 2 Observation modes of the MEP-i

Mode	Size (Byte)	Data	Notes
Normal	4096	16-bit counter × 16 × 16 × 8 (SV, AZ, TOF)	8 TOF groups are sorted using the *m/q* tables
	640	32-bit list data, 160 events at maximum	
TOF	4096	16-bit counters: × 4 × 512 (AZ, TOF)	
	48	24-bit counters (start only) × 16 (AZ)	For in-flight calibration
	48	24-bit counters (stop only) × 16 (AZ)	For in-flight calibration
	48	24-bit counters (double coincidence) × 16 (AZ)	For in-flight calibration
	640	32-bit list data, 160 events at maximum	PH is not available
SSD	4096	16-bit counter × 16 × 8× 16 (SV, AZ, E)	TOF is not available
	640	32-bit list data, 160 events at maximum	

SV, AZ, TOF, and PH indicate the sweeping voltage, azimuthal angle, time-of-flight, and pulse height, corresponding to the *E/q*, incident direction, *m/q*, and *E*, respectively. The 32-bit list data contains the values of SV (4 bits), AZ (4 bits), TOF (9 bits), and PH (10 bits)

Table 3 Data reduction modes of the MEP-i

Mode	Notes
Raw	No reduction
Superposition	*N*-spin accumulated where $N = 2^i (i = 1, 2, 3)$ and *i* can be determined by commands
Snapshot	Non-reduced full spin data are obtained once per *N* spins, while the other $(N - 1)$-spin data are discarded where $N = 2^i (i = 1, 2, 3)$ and *i* can be determined by commands
Spin-phase mask	Only 1-spin-phase data are derived from *N*-spin-phase data, where $N = 2^i (i = 1, 2, 3)$ and *i* can be determined by commands

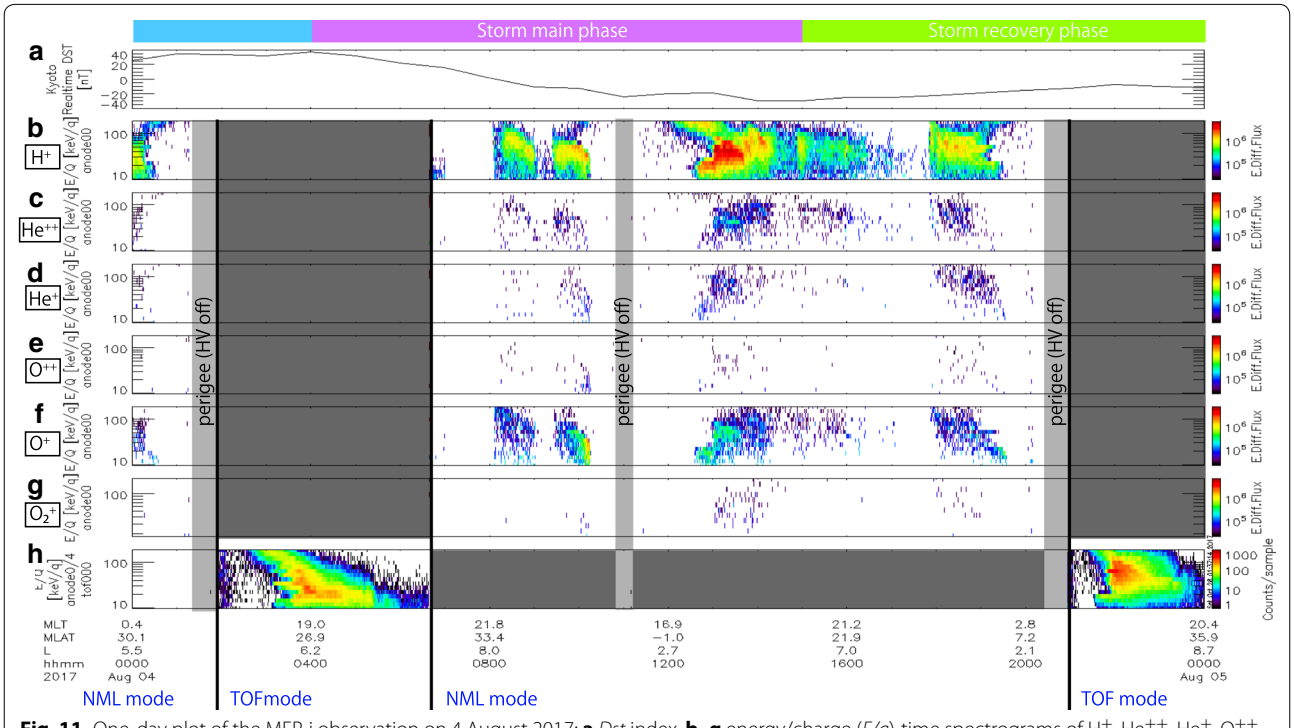

Fig. 11 One-day plot of the MEP-i observation on 4 August 2017; **a** *Dst* index, **b**–**g** energy/charge (*E/q*)-time spectrograms of H^+, He^{++}, He^+, O^{++}, O^+, and O_2^+ obtained in the Normal mode, and **h** *E/q*-time spectrogram of all ion species in the TOF mode. The colors indicate the energy differential flux (keV/cm^2 sr keV s)

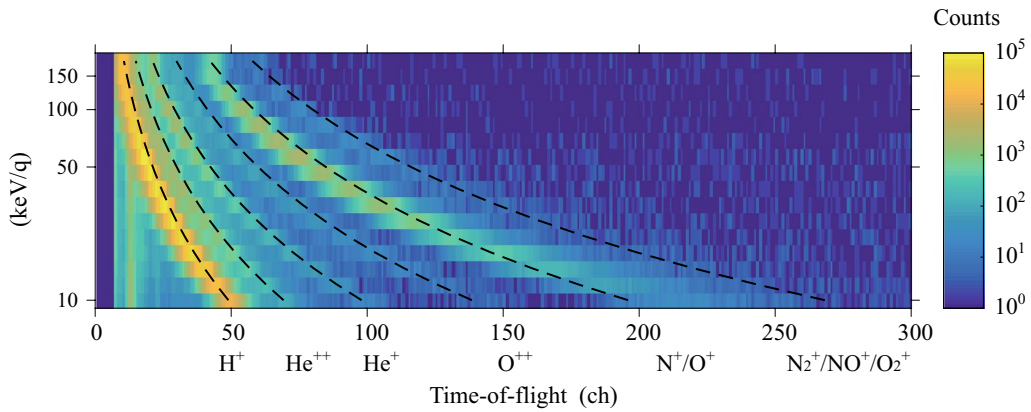

Fig. 12 TOF-energy/charge (*E/q*) profile of ions measured by the MEP-i on August 4, 2017. The dashed lines indicate the central TOF for H^+ ($m/q = 1$), He^{++} ($m/q = 2$), He^+ ($m/q = 4$), O^{++} ($m/q = 8$), N^+/O^+($m/q = 14$–16), and $N_2^+/NO^+/O_2^+$ ($m/q = 28$–32) based on *E/q* measurements. A unit of the TOF channel corresponds to 0.78125 ns

as those in the other modes. The SSD mode was prepared mainly for in-flight calibration. The list data are also included, while the TOF information is not available.

Table-dump mode

The sensor tables for the SV step and *m/q* are dumped instead of the count data. No scientific data are acquired in this mode. This mode is mainly used for checking the table data after replacing them.

Operation and flight performance

The MEP-i was turned-on on February 1, 2017, for the initial functional check. Commissioning testing of the MEP-i high-voltage power supplies was conducted in mid-February. On 23 March, the MEP-i as well as the other science instruments started nominal observation. Since the maximum SVs applied to the ESA unit are relatively high (± 5 kV), we conservatively limited the uppermost SV values at ± 3 kV (the corresponding maximum energy is ~ 110 keV/q) until the end of the first observation campaign. On 22 April, the MEP-i observation in the energy range up to 180 keV/q started by applying the SVs up to ± 5 kV.

The MEP-i has been operated in Normal and TOF modes. Figure 11 shows 1-day plots on August 4, 2017,

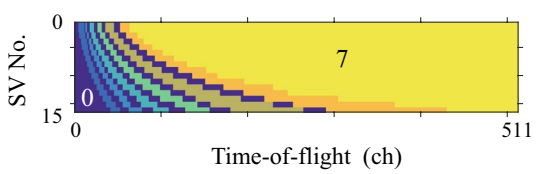

Fig. 13 Mass-per-charge (*m/q*) table of the 16 SV steps and 512 TOF channels used for the allocation of the 8 *m/q* bins in the Normal mode. The 8 colors indicate the *m/q*-bin number

when a moderate magnetic storm (*Dst* index ~ − 40 nT) occurred (see Fig. 11a). The observation was regularly suspended around the perigee (1:30, 11:00, and 20:30 UT on this day) in order to avoid damage to the detector by penetrating protons (> 50 MeV). The TOF mode started at 1:30 and 20:30 UT, following the perigee passes. On this day, the ascending pass from perigee to apogee was operated in the TOF mode, while the descending pass from apogee was in the Normal mode, except for the second pass, where the Normal mode was used in conjunction with other space probes.

The Normal mode provides energy/charge (*E/q*)-time spectrograms for several ion species, and Fig. 11b nominally illustrates that of H^+, while Fig. 11c–g shows those of He^{++}, He^+, O^{++}, O^+, and O_2^+, respectively. It is clearly demonstrated that the fluxes of heavy ions were particularly enhanced during the main and early recovery phases of the storm. Another result of high activity during this period is the measurement of successive energy–time dispersion signatures which spread over the medium energy range, especially around 14–16 UT. It seemed as though more He^{++} appeared in the storm than He^+, possibly due to the solar wind contribution (Kremser et al. 1993, 1994). However, in the Normal mode, the bin for He^{++} could be contaminated by a large amount of H^+. For investigating the He^{++}/He^+ ratio in future works, detailed studies using the list data and TOF-mode data are required.

The omni-ion *E/q*-time spectrogram obtained in the TOF mode is also plotted at intervals of the spin period (~ 8 s) in Fig. 11h. The omni-ion *E/q*-time spectrogram of the TOF mode did not contain all combinations of *E/q* and direction, as described in "TOF mode" subsection.

The TOF mode also provides the *E/q*-TOF profiles as shown in Fig. 12. On this day, the MEP-i observed H^+,

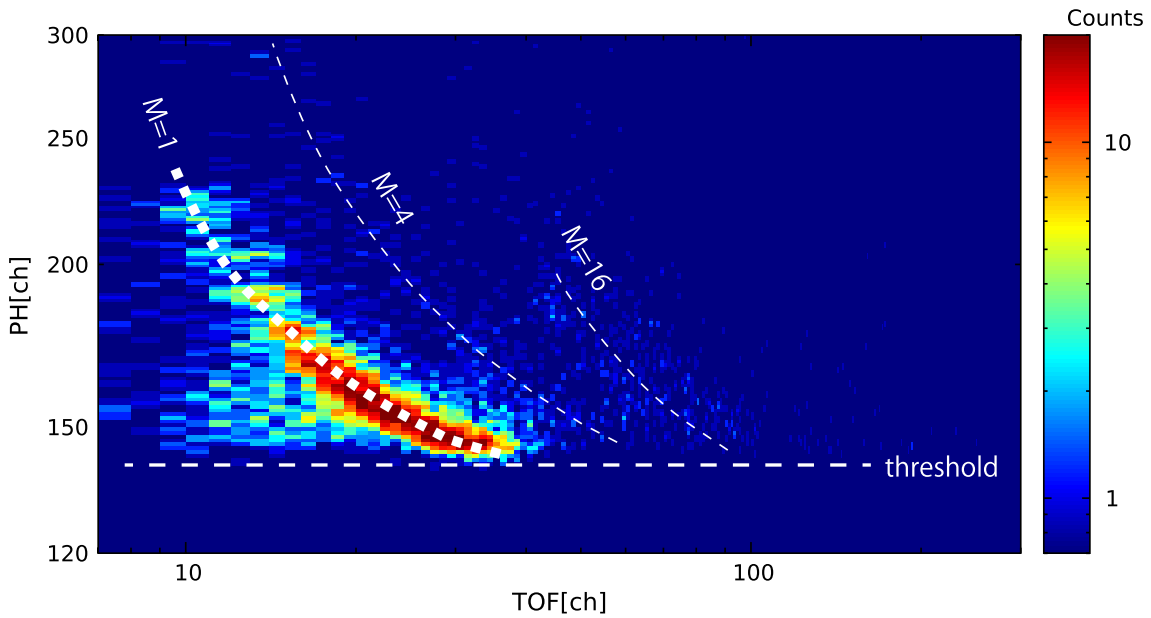

Fig. 14 TOF-PH (corresponding *E*) profile of ions measured by the MEP-i during 8–16 UT on August 4, 2017. The profile was derived from the list data in the Normal mode

He^{++}, He^{+}, O^{++}, O^{+}, and $O_2{}^{+}$. N^{+} was not clearly discriminated from O^{+}, at least in this plot, while it has been detected several times in the inner magnetosphere (Christon et al. 2002; Liu et al. 2005). However, since the TOF profiles of N^{+} and O^{+} were measured in the laboratory, detailed analyses in the future may enable us to estimate the N^{+} fluxes. The MEP-i also detected molecular ions which were most likely $O_2{}^{+}$, possibly including $N_2{}^{+}$ and NO^{+}. As previous reports on such molecular ions are insufficient (Klecker et al. 1986; Yau et al. 1993; Peterson et al. 1994), it is expected that MEP-i observations will provide more information regarding molecular ion behaviors (e.g., dependence on L-value, magnetic local time, and solar activity) to reveal the escaping mechanisms of the Earth's atmospheric particles.

In addition, for the allocation of the 8 *m/q* bins in the Normal mode, we prepared the *m/q* table by using the *E/q*-TOF profiles obtained in the TOF mode. Figure 13 shows the latest *m/q* table of the 16 SV steps and 512 TOF channels, which were used for the data plotted in Fig. 11.

Finally, the PH profiles from the SSD detection are investigated. Figure 14 shows the PH-TOF response derived from the list data on 4 August 2017. The most intense signature is due to H^{+} ($m = 1$), while He^{+}/He^{++}($m = 4$) and O^{+} ($m = 16$) produce relatively weak counts. Although the PH-TOF response is similar to the *E/q*-TOF profile in Fig. 11, the PH-TOF response provides *m* rather than *m/q*, because the PH information indicates *E* (not *E/q*). The PH-TOF response also shows an agreement with the laboratory results in which we estimated a PH zero energy of ~ 140, discrimination level of ~ 143, and conversion factor of ~ 2 keV/unit.

Summary

The MEP-i has successfully started measurements of the three-dimensional distribution functions for H^{+}, He^{++}, He^{+}, O^{++}, and N^{+}/O^{+} in the medium energy range (10–180 keV/q) in the Earth's inner magnetosphere. Molecular ions ($O_2{}^{+}$, and possibly $N_2{}^{+}$ and NO^{+}) were also measured during some storm times. Observations of the MEP-i with other instruments onboard ERG, and in conjunction with other spacecraft and ground stations will provide us with comprehensive information on the ion dynamics in the inner magnetosphere and its role in radiation belt electron dynamics.

Authors' contributions

SY and SK developed the instrument, wrote the manuscript, and analyzed the data. SY, SK, TM, KA, MH, TT, KY, and YS contributed to the development and observation. All authors read and approved the final manuscript.

Author details

[1] Osaka University, Machikaneyama-cho, Toyonaka 560-0043, Japan. [2] The University of Tokyo, Hongo, Bunkyo-ku 113-0033, Japan. [3] Institute of Space and Astronautical Science, Japan Aerospace Exploration Agency, Yoshinodai, Chuo-ku, Sagamihara 252-5210, Japan. [4] Institute for Space-Earth Environmental Research, Nagoya University, Furo-cho, Chikusa-ku, Nagoya 464-8601, Japan. [5] Kyoto University, Kitashirakawaoiwake-cho, Sakyo-ku, Kyoto 606-8502, Japan.

Acknowledgements
The authors would like to express sincere thanks to all members of the ERG mission for their supports and operations. The authors would like to thank Dr. L. Kistler for helpful comments. The MEP-i components were manufactured by Meisei Electric Co., Ltd., Mitsubishi Heavy Industries, Ltd., Hamamatsu Photonics K. K. and YS design.

Competing interests
The authors declare that they have no competing interests.

Availability of data and materials
The data and materials used in this research are available on request to the corresponding author, Dr. Shoichiro Yokota (yokota@ess.sci.osaka-u.ac.jp). The ERG (Arase) satellite science data will be available at https://ergsc.isee.nagoya-u.ac.jp/index.shtml.en (ERG Science Centre operated by ISAS/JAXA and ISEE/Nagoya University). The *Dst* index is available at http://wdc.kugi.kyoto-u.ac.jp/dstdir/index.html.

Publisher's Note

Received: 30 August 2017 Accepted: 5 December 2017
Published online: 21 December 2017

References

Asamura K, Kazama Y, Yokota S, Kasahara S, Miyoshi Y. Low-energy particle experiments-ion analyzer (LEP-i) onboard the ERG (Arase) satellite **(in preparation)**

Boardsen SA, Gallagher DL, Gurnett DA, Peterson WK, Green JL (1992) Funnel-shaped low-frequency equatorial waves. J Geophys Res 97:14967–14976

Carlson CW, Curtis DW, Paschmann G, Michel W (1982) An instrument for rapidly measuring plasma distribution functions with high resolution. Adv Sp Res 2(7):67–70

Chen L, Thorne RM, Jordanova VK, Horne RB (2010) Global simulation of magnetosonic wave instability in the storm time magnetosphere. J Geophys Res 115:A11222. https://doi.org/10.1029/2010JA015707

Christon SP, Mall U, Eastman TE, Gloeckler G, Lui ATY, McEntire RW, Roelof EC (2002) Solar cycle and geomagnetic N^{+1}/O^{+1} variation in outer dayside magnetosphere: possible relation to topside ionosphere. Geophys Res Lett 29(5):1058. https://doi.org/10.1029/2001GL013988

Delcourt D et al (2016) The Mass Spectrum Analyzer (MSA) on board the BepiColombo MMO. J Geophys Res Space Phys. https://doi.org/10.1002/2016JA022380

Dessler AJ, Karplus R (1961) Some effects of diamagnetic ring currents on Van Allen radiation. J Geophys Res 66(8):2289–2295. https://doi.org/10.1029/JZ066i008p02289

Funsten HO, Ritzau SM, Harper RW, Korde R (2004) Fundamental limits to detection of low-energy ions using silicon solid-state detectors. Appl Phys Lett 84(18):2554–3552

Gloeckler G et al (1992) Solar wind ion composition spectrometer. Astron Astrophys Suppl Ser 92:267–289

Hamilton DC, Gloeckler G, Ipavich FM, Lundgren RA, Sheldon RB, Hovestadt D (1990) New high-resolution electrostatic ion mass analyzer using time of flight. Rev Sci Instrum 61:3104–3106

Horne RB, Thorne RM (1998) Potential waves for relativistic electron scattering and stochastic acceleration during magnetic storms. Geophys Res Lett 25:3011–3014

Horne RB, Thorne RM, Glauert SA, Meredith NP, Pokhotelov D, Santolk O (2007) Electron acceleration in the Van Allen radiation belts by fast magnetosonic waves. Geophys Res Lett 34:L17107

Kasahara S, Asamura K, Saito Y, Takashima T, Hirahara M, Mukai T (2006) Cusp type electrostatic analyzer for measurements of medium energy charged particles. Rev Sci Instrum 77:123303

Kasahara S, Mitani T, Ogasawara K, Takashima T, Hirahara M, Asamura K (2009) Application of single-sided silicon strip detector to energy and charge state measurements of medium energy ions in space. Nucl Instrum Methods Phys Res Sect A 603(3):355–360

Kasahara Y et al (2017) The Plasma Wave Experiment (PWE) on board the Arase (ERG) Satellite. Earth Planets Space. http://doi.org/10.1186/s40623-017-0759-3

Kazama Y et al (2017) Low-energy particle experiments–electron analyzer (LEPe) onboard the Arase spacecraft. Earth Planets Space 69:165. https://earth-planets-space.springeropen.com/articles/10.1186/s40623-017-0748-6

Kennel CF, Petschek HE (1966) Limit on stably trapped particle fluxes. J Geophys Res 71(1):1–28. https://doi.org/10.1029/JZ071i001p00001

Kitamura N, Seki K, Nishimura Y, Terada N, Ono T, Hori T, Strangeway RJ (2012) Photoelectron flows in the polar wind during geomagnetically quiet periods. J Geophys Res 117:A07214

Klecker B, Möbius E, Hovestadt D, Scholer M, Gloeckler G, Ipavich FM (1986) Discovery of energetic molecular ions (NO^+ and O_2^+) in the storm time ring current. Geophys Res Lett 13(7):632–635

Kremser G, Wilken B, Gloeckler G, Hamilton DC, Ipavich FM, Kistler LM, Tanskanen P (1993) Origin, transport, and losses of energetic He^+ and He^{++} ions in the magnetosphere of the Earth: AMPTE/CCE observations. Ann Geophys 11:354–365

Kremser G, Rasinkangas R, Tanskanen P, Wilken B, Gloeckler G (1994) Solar wind contribution to the average population of energetic He^+ and He^{++} ions in the Earth's magnetosphere. Ann Geophys 12(2–3):152–168

Liu WL, Fu SY, Zong Q-G, Pu ZY, Yang J, Ruan P (2005) Variations of N^+/O^+ in the ring current during magnetic storms. Geophys Res Lett 32:L15102. https://doi.org/10.1029/2005GL023038

MacDonald EA et al (2009) New magnetospheric ion composition measurement techniques. AIP Conf Proc 1144:168

McComas DJ et al (2013) The Jovian auroral distributions experiment (JADE) on the Juno Mission to Jupiter. Space Sci Rev. https://doi.org/10.1007/s11214-013-9990-9

Miyoshi Y et al. Geospace exploration project ERG: overview (**in preparation**)

Miyoshi Y, Sakaguchi K, Shiokawa K, Evans D, Albert J, Connors M, Jordanova V (2008) Precipitation of radiation belt electrons by EMIC waves, observed from ground and space. Geophys Res Lett 35:L23101. https://doi.org/10.1029/2008GL035727

Peterson WK et al (1994) On the sources of energization of molecular ions at ionospheric altitudes. J Geophys Res 99(A12):23257–23274

Shoji M, Omura Y (2011) Simulation of electromagnetic ion cyclotron triggered emissions in the Earth's inner magnetosphere. J Geophys Res 116:A05212. https://doi.org/10.1029/2010JA016351

Su Y-J, Horwitz JL, Wilson GR, Richards PG, Brown DG, Ho CW (1998) Self-consistent simulation of the photoelectron-driven polar wind from 120 km to 9 R_E altitude. J Geophys Res 103:2279–2296

Summers D, Thorne RM, Xiao F (1998) Relativistic theory of wave-particle resonant diffusion with application to electron acceleration in the magnetosphere. J Geophys Res 103:20487–20500

Williams CW, Kiker WE, Schmitt HW (1964) Correlated energy and time-of-flight measurements of fission fragments with semiconductor detectors: system design and performance. Rev Sci Instrum 35:1116–1123

Williams DJ, Keppler E, Fritz TA, Wilken B, Wibberenz G (1978) The ISEE 1 and 2 medium energy particles experiment. ISEE Trans Geosci Electron 16:278–280

Wilson GR, Khazanov G, Horwitz JL (1997) Achieving zero current for polar wind outflow on open flux tubes subjected to large photoelectron fluxes. Geophys Res Lett 24:1183–1186

Yau AW, Whalen BA, Goodenough C, Sagawa E, Mukai T (1993) EXOS D (Akebono) observations of molecular NO^+ and N_2^+ upflowing ion in the high-altitude auroral ionosphere. J Geophys Res 98(A7):11205–11224

Yokota S, Saito Y, Asamura K, Mukai T (2005) Development of an ion energy mass spectrometer for application on board three-axis stabilized spacecraft. Rev Sci Instrum 76:014501–014508.

Young DT, Bame SJ, Thomsen MF, Martin RH, Burch JL, Marshall JA, Reinhard B (1988) 2π-radian field-of-view toroidal electrostatic analyzer. Rev Sci Instrum 59:743. https://doi.org/10.1063/1.1139821